Cardiac-Gated Spectroscopic Photoacoustic Imaging for Ablation-Induced Necrotic Lesion Visualization: *In Vivo* Demonstration in a Beating Heart

Shang Gao[a], Hiroshi Ashikaga[d], Masahito Suzuki[d], Tommaso Mansi[g], Young-Ho Kim[g], Florin-Cristian Ghesu[g], Jeeun Kang[e,f], Emad M. Boctor[e,f], Henry R. Halperin[d], Haichong K. Zhang[a,b,c*]

[a]Robotics Engineering Department, [b]Biomedical Engineering Department, [c]Computer Science Department, Worcester Polytechnic Institute, Worcester, MA, United States of America

[d]Division of Cardiology, Department of Medicine, [e]Department of Radiology and Radiological Science, Johns Hopkins University School of Medicine, Baltimore, MD, United States of America

[f]Laboratory for Computational Sensing and Robotics, Whiting School of Engineering, Johns Hopkins University, MD, United States of America

[g]Digital Technology and Innovation, Siemens Healthineers, Princeton, NJ, United States of America

*hzhang10@wpi.edu

Abstract

Radiofrequency (RF) ablation is a minimally invasive therapy for heart arrhythmia including atrial fibrillation (A-fib) by creating lesions to isolate the heart from abnormal electrical signals using an electric current. However, conventional RF procedures do not involve intraoperative monitoring of the area and extent of ablation-induced necrosis, making the assessment of procedure completeness challenging. Previous studies have suggested that spectroscopic photoacoustic (sPA) imaging is capable of differentiating ablated tissue from its non-ablated counterpart based on their PA spectrum variation. Here, we aim to demonstrate the applicability of sPA imaging in an *in vivo* environment where the cardiac motion presents and introduce a framework for mapping the necrotic lesion based on cardiac-gated sPA imaging. We computed the degree of necrosis (necrotic extent, NE) by taking the fraction of the quantified ablated tissue contrast over the total contrast from both ablated and non-ablated tissues, visualizing it as continuous colormap to highlight the necrotic area and extent. To compensate the tissue motion during a cardiac cycle, we applied the cardiac-gating on sPA data based on the image similarity. The *in vivo* validation of the concept was conducted in a swine model. As a result, the ablation-induced necrotic lesion at the surface of a beating heart was depicted throughout a cardiac cycle through cardiac-gated sPA (CG-sPA) imaging. The measured necrotic region geometry across the entire cardiac cycle was 6.01 ± 2.35 mm in width by 1.79 ± 0.75 mm in depth, which was comparable to the gross pathology with 6.0 mm by 2.9 mm, respectively. The results suggest that the introduced CG-sPA imaging system has the great potential to be incorporated into clinical workflow to guide ablation procedures intraoperatively.

Keywords spectroscopic photoacoustic imaging, cardiac-gating, cardiac ablation, image-guided intervention, *in vivo* demonstration,

1. Introduction

Atrial Fibrillation (A-fib) is the most common type of heart arrhythmia [1]. In A-fib, the left and right atriums receive chaotic bioelectronic signals, causing an irregular and often rapid heart rate. A-fib could

induce blood clots in the heart and increase the risk of stroke, heart failure, and other heart-related complications. Between 2.7 and 6.1 million patients are currently affected by A-fib in the United States. According to the CDC, this number is estimated to rise to 12.1 million by 2030 [2]. The current standard of care for drug-resistant A-fib percutaneous catheter ablation therapy includes radiofrequency (RF) ablation. It aims to create lines of targeted tissue necrosis surrounding the pulmonary veins by creating lesions that protect the heart from abnormal electrical signals originating from the pulmonary veins to trigger A-fib. However, the lack of intraoperative evaluation of ablated tissues causes inadequate and excessive ablation. A-fib recurrence within the first year after the operation is common and greatly associated with inadequate ablation [3]. Excessive ablation could lead to steam pop, a relatively infrequent (0.1% to 1.5%) but potentially severe complication [4,5]. Steam pop has been associated with embolic strokes, cardiac perforations, and ventricular septal defects. While imaging modalities such as magnetic resonance imaging (MRI) and computed tomography (CT) are clinically used to assess ablated lesions, both modalities do not provide real-time feedback, and their intraoperative usage is still in its infancy. Monitoring the necrotic lesion formation intraoperatively is critical to prevent excessive or incomplete ablation.

Photoacoustic (PA) imaging is an emerging imaging modality based on laser-generated ultrasound, depicting tissue optical absorption [6–8]. Different materials possess unique spectroscopic characteristics and those can be used to characterize different types of chromophores [9,10]. The imaging modality has been widely used for vascular mapping [11–15], tumor detection [16–18], and oxygenation mapping [19,20]. The implementation of PA imaging has been investigated in intravascular imaging for vulnerable plaques detection [21–25], as well as the intraplaque hemorrhages in carotid artery plaque [26,27]. The PA imaging was reported on cardiac arrhythmia as well. Graham et al. reported a PA-based localization of the cardiovascular catheter by attaching an optical fiber to generate a beacon PA signal from the tip of the catheter [28]. The monitor of the RF ablation using PA imaging was also reported in the previous works. It was reported that the PA spectrum of ablated tissues is different from that of non-ablated tissues [29,30]. The ablated tissue contrast could be highlighted with respect to surrounding non-ablated counterparts through spectroscopic PA (sPA) imaging. Iskander-Rizk et al. demonstrated the real-time implementation of cardiac ablation monitoring by visualizing the intensity ratio of two-wavelength PA data in an *ex vivo* setting [31–33]. Although the abovementioned works made a substantial contribution to suggesting the feasibility of sPA imaging for ablated lesion evaluation, the assessment of lesion continuity and ablation extent are challenging by mapping the ablated tissue contrast alone because weak ablated tissue contrast that attributed to no sufficient light illumination or viable tissue is indistinguishable. Effective visualization of the lesion boundary between ablated and non-ablated tissues is vital for providing accurate feedback to guide the intraoperative ablation procedure. More importantly, the cardiac applicability of the sPA imaging in an *in vivo* environment has not been demonstrated. The dynamic heartbeat motion and interference from other contrasts such as blood are expected to negatively impact the sPA imaging performance.

In this paper, we introduce a framework mapping the extent of tissue necrosis based on sPA imaging with cardiac gating incorporated to explore the applicability of the sPA ablation monitoring in an *in vivo* environment. We computed the degree of necrosis (necrotic extent, NE) by taking the fraction of the quantified ablated tissue contrast over the total contrast from both ablated and non-ablated tissues, visualizing it as continuous colormap to highlight the necrotic area and extent. To compensate the tissue motion during a cardiac cycle, we applied the cardiac-gating on sPA data based on the image similarity. The concept is validated in the *in vivo* swine model, assessing the ablation-induced necrotic lesion on the beating heart surface.

This paper first introduces the methodology for computing necrotic extent (NE) mapping and image similarity-based cardiac gating algorithm for cardiac motion compensation. Then, the experimental setup and animal preparation for *in vivo* validation are described. The results present the imaging performance compared with the control groups and the system tolerance with limited PA data to evaluate the potential for real-time implementation. Finally, the findings from the study and limitations are discussed.

2. Materials and Methods

2.1. Necrotic Extent Mapping

We introduce a necrotic region mapping method, quantifying the extent of ablation-induced necrosis with respect to the non-necrotic tissue. After decomposing the contrast of two myocardium states, the necrotic extent (NE) will be quantified based on the contribution from the necrotic tissue contrast with respect to the total contrast combined with that of non-necrotic tissue.

Biomedical materials each have unique optical absorption characteristics consisting of PA spectra. The measured PA signals are consisted by the combination of contrasts from multiple chromophores and contrast agents. Decomposing each material contribution and forming an sPA image can be conducted through spectroscopic decomposition (also known as material decomposition or spectral unmixing) [34]. Such a technology has been well explored in blood oxygenation mapping [35] and contrast agent enhanced imaging [34]. Based on the assumption that the received PA spectrum consists of a linear combination of multiple chromophores, the contribution from each contrast is estimated as Eq. (1) [34].

$$\underset{m_{1,2,\ldots,M}}{\text{Argmin}} \left\| \sum_{W} \left(p - \sum_{i=1}^{M} m_i \mu_{a,i} \right)^2 \right\| \tag{1}$$

where p is the measured PA spectrum, i is the contrast source number, M is the number of absorbers, μ_a is the absorption spectrum of contrast i, and W presents the wavelengths used.

In this proposed work, we first implemented spectroscopic decomposition to distinguish the contribution of the contrast of the ablated tissue from that of the non-ablated tissue. With the reference PA spectra from ablated and non-ablated tissues as the input, the contrast contribution from two tissue types is decomposed. Figure 1 shows the PA spectra used in this study, obtained from our previous work with the swine model [36]. An equivalent spectral trend is observed in the work reported by Dana et al [30].

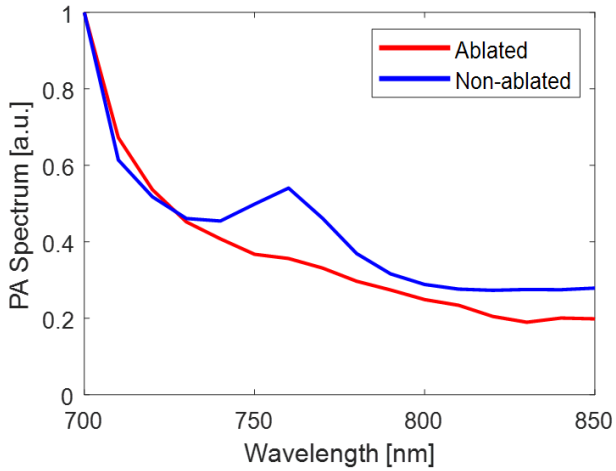

Figure 1. The PA spectrum from ablated and non-ablated tissues used for spectroscopic decomposition [36].

The second step of quantifying the extent of tissue necrosis is to estimate the contribution of the ablated tissue contrast with respect to the combination with the non-ablated tissue contrast based on the decomposed contrast from both ablated and non-ablated tissue types. This is based on the assumption that non-necrotic tissue should not contain the contrast from the ablated tissue and fully ablated necrotic tissue should not contain that from the non-ablated tissue. The necrotic extent (NE) metric presents the intensity ratio between ablated tissue contrast (m_{Ab}) and the summation of ablated tissue contrast with non-ablated tissue ($m_{N\text{-}Ab}$), as shown in Eq. (2). Such a mapping method is capable of capturing the transition between two tissue statuses.

$$NE = \frac{m_{Ab}}{m_{Ab} + m_{N-Ab}} \tag{2}$$

In addition, it is required to account for the potential occurrence of insufficient light illumination during scanning and the presence of background noise. In such case, the measured PA spectrum will contain signals non-specific to neither ablated nor non-ablated tissue spectra, which could affect the estimation accuracy of both ablated and non-ablated tissue contrasts. Therefore, we regard those non-specific signal spectra as residual and filter out the pixel containing high residual contrast with respect to the total PA contrast to only visualize the contrast with higher confidence in NE mapping, as:

$$\frac{\sum_W \left(p - \sum_{i=1}^{M} m_i \mu_{a,i}\right)}{\sum_W p} < R_{thres} \tag{3}$$

where R_{thres} is the residual threshold value which is set at 0.2 in this work. This threshold enhances the tissue contrast in the scanned image by differentiating the low-intensity PA signal generated by the tissue from noise signals. The output NE map is displayed with a continuous colormap to show the transition of tissue necrosis in an intuitive visual sense, in which red indicates ablated and blue indicates non-ablated tissues, respectively. The NE value of 0.2 was set for defining the boundary of the ablated region.

2.2. Cardiac-Gated Spectroscopic Photoacoustic (CG-sPA) Imaging

The imaging speed of sPA imaging is determined by factors such as the laser pulse repetition frequency (typically 10-20 Hz or at most 100 Hz) and the number of wavelengths used for spectroscopic

decomposition. Additionally, the signal-to-noise ratio (SNR) of the PA signals in the *in vivo* environment is expected to be compromised due to the limited space for placing light delivery fibers and light absorption from blood, requiring frame averaging to enhance the SNR. Hence, a certain temporal duration of PA data is required for sPA imaging in an intracardiac environment. However, continuous drastic tissue motion due to heartbeat introduces severe motion artifacts and prevents direct data processing, motivating us to introduce cardiac gating to enable in vivo sPA imaging of a beating heart. Specifically, we track and map the recorded PA data to a specific time point with respect to a cardiac cycle. The image similarity with respect to the specific time point is used to sort and align PA data, in which averaging filter and spectral decomposition, and necrotic extent mapping are applied.

To track the temporal variation and similarly of PA images over time, we computed the 2D cross-correlation coefficient of two PA image frames. The coefficient, R, was defined in Eq (4) as a scalar value between 0 and 1, of which 1 suggests two input images are identical, and 0 indicates the opposite. The variable m, n is the pixel number in the input 2D envelope detected PA images A and B, and $\overline{A}$ and $\overline{B}$ represent the mean value of A and B intensity.

$$R = \frac{\sum_m \sum_n \left(A_{mn} - \overline{A}\right)\left(B_{mn} - \overline{B}\right)}{\sqrt{\left(\sum_m \sum_n \left(A_{mn} - \overline{A}\right)^2\right)\left(\sum_m \sum_n \left(B_{mn} - \overline{B}\right)^2\right)}} \tag{4}$$

Based on the similarity between any two PA imaging frames, a high cross-correlation coefficient indicates the two cardiac PA images were taken when the cardiac tissue appears at a similar location in the field of view (FOV). Yet, the high coefficient, R, alone is not sufficient to extract a cardiac cycle because the tissue surface passes a similar location in the imaging FOV twice in a cardiac cycle during the contraction and relaxation. The contraction and relaxation data should be distinguished because the muscle status of the cardiac tissue could be different between them. This could introduce additional noise in the spectrum when images were averaged. Therefore, we categorized the PA frames that based on not only the image similarity but also the isolation between the contraction and relaxation phases in a cardiac cycle.

To examine the similarity alignment of two frames with respect to a cardiac cycle, we computed the image correlation coefficient in the temporal axis. The temporal correlation coefficient was defined as R_T shown in Eq. (5), where R is the correlation coefficient defined in Eq. (4) which evaluated the similarity of PA image frame f with respect to a reference frame f^r. The correlation coefficient of the frame i was compared, as well as the frames (i - j) in the previous cardiac cycle with the length of M image frame. The sorted high R_T frames guarantee both similarities in tissue position in the image FOV and the alignment with respect to a cardiac cycle.

$$R_T = \frac{\sum_j^M R(f_{i-j}, f_{i-j}^r)}{M} \tag{5}$$

The aligned PA images at the same timing in a cardiac cycle were averaged to offer SNR-improved cardiac-gated (CG) PA images.

Figure 2 summarizes the workflow of signal processing for the recorded PA images with the proposed CG-sPA imaging incorporating both cardiac gating and spectroscopic decomposition. The acquired PA channel data were first beamformed by Delay-and-Sum (DAS) algorithm [37] and envelope detected and then sorted based on their PA excitation wavelengths. In each sorted wavelength frame set, a routine of the cardiac tissue surface motion was observed and it was tracked with R_T to a defined reference frame in a particular cardiac cycle. At each stage of the CG, the R_T of all the recorded PA frames was calculated with respect to the reference frame at this cardiac cycle. Frames with calculated R_T above the threshold (defined as 0.4 in our work) were selected and averaged. The same process was applied to all individual illuminated wavelength data. The SNR enhanced outputs through averaging at each wavelength were combined as a CG sPA data set for the following spectroscopic decomposition to distinguish ablated and non-ablated

tissue spectrums. The NE map was computed as described in the previous section. The process was then repeated to the frames throughout a cardiac cycle.

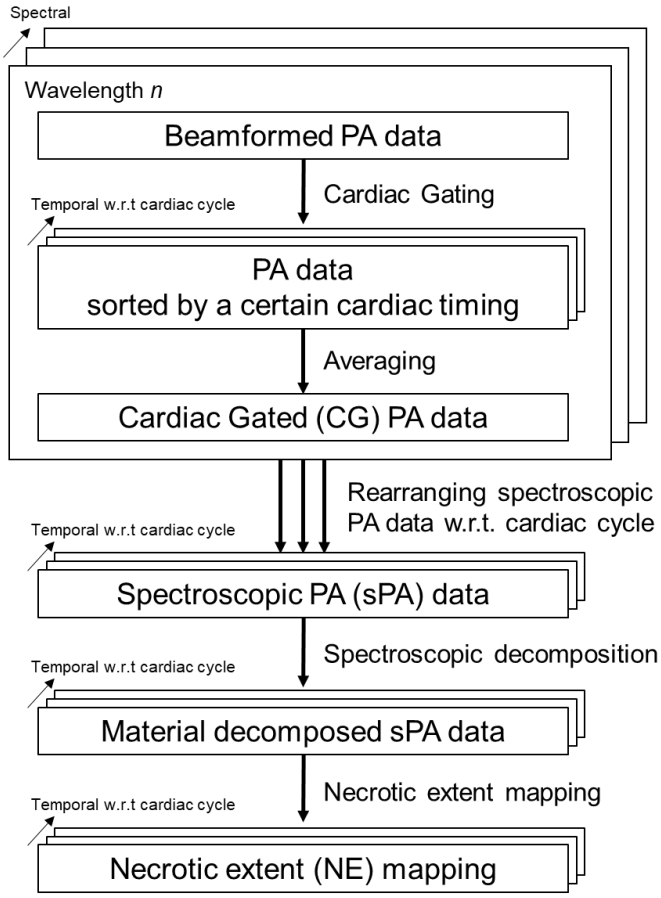

Figure 2. Cardiac-gated spectroscopic PA (CG-sPA) image processing flowchart

3. Implementation

3.1. Experimental Setup

The PA imaging system setup used is shown in Figure 3 (a). A 128 elements linear-array ultrasound (US) transducer probe (Philips ATL Lap L9-5, Philips, Netherlands) was used as the ultrasound receiver. The Verasonics Vantage system (Vantage 256, Verasonics, USA) was used as the data acquisition device. A Q-switched Nd:YAG laser (Q-smart 450, Quantel, USA) with an optical parametric oscillator (OPO) (MagicPRISM, OPOTEK, USA) was used, which is capable of generating a laser pulse at the wavelength range of 690-950 nm at a repetition rate of 20 Hz with 5 ns pulse duration.

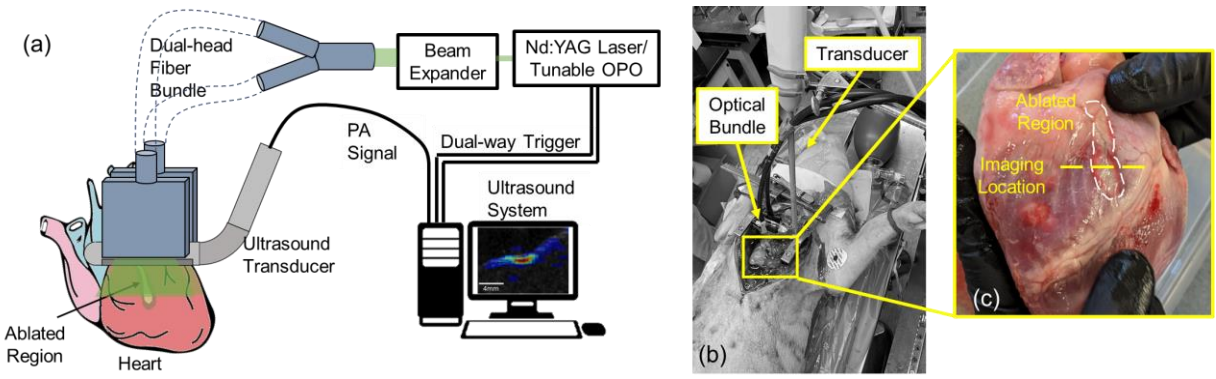

Figure 3. (a) The sketch of the imaging setup and system architecture (b) *In vivo* cardiac PA imaging setup with swine model, (c) The post-procedure heart surface with the ablated region highlighted. The yellow dot-line indicates the imaging slice for necrotic detection.

We implemented two illumination modes for sPA imaging as illustrated in Figure 4. Three-wavelength Repetitive Illumination (3WL_Rep), allows a fast wavelength tuning between pre-defined sets of wavelengths. There is no tuning delay between wavelengths and continuous scanning at 20 Hz repetition rate is achievable. In this study, 740 nm, 760 nm and 780 nm wavelength laser was used and repetitively illuminated to acquire sPA image. This mode is suitable to achieve a high frame range of sPA imaging based on the limited number of wavelengths. The other mode, Sixteen-wavelength Individual Illumination (16WL_Indiv) allows a range of laser wavelengths with a defined step size. 700 nm to 850 nm wavelength laser was used with 10 nm step. 64 frames of PA data were scanned at each wavelength. Having access to a higher number of wavelengths offers a more robust spectroscopic decomposition, suitable for cross-validation of the fast scanning mode.

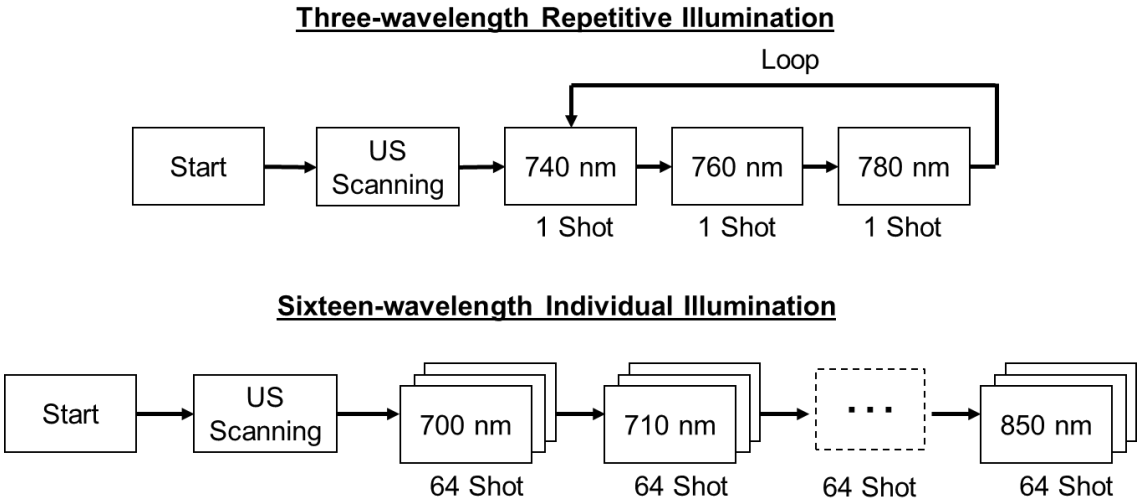

Figure 4. Two laser illumination modes. Three-wavelength repetitive illumination (3WL_Rep) is suitable to achieve a high frame sPA imaging. Sixteen-wavelength Individual Illumination (16WL_Indiv) offers a robust spectroscopic decomposition.

3.2 Animal Preparation and Study Procedure

A swine was prepared for a cardiac ablation procedure approved by the Johns Hopkins Animal Care and Use Committee (Protocol SW20M200). The swine was initially anesthetized with mechanical ventilation using a combination of ketamine and xylazine and maintained under sedation using 1–2% isoflurane. The swine was shaved, and its chest was opened to expose the heart for ablation and imaging. The subject was positioned supine as shown in Figure 3 (b) and was continuously monitored throughout the procedure. Ablation was performed using an irrigated 3.5 mm-tip ablation catheter (FlexAbility, Abbott, USA) on a part of the cardiac tissue surface as shown in Figure 3 (c). The RF ablation was delivered at 30W with a temperature limit of 48 °C. The irrigation speed was 17 mL/min. A line of the ablated tissue region was created so that the cross-sectional PA image can capture the ablated area. The PA imaging system was placed at the top of the chest while insuring the ablated area was within the FOV (Figure 3 (b)). Ultrasounds gel (Aquasonic Clear Ultrasound Transmission Gel, Parker Laboratories, USA) was filled between the cardiac surface and the transducer to transmit the acoustic signal.

The experimental conditions were summarized in Table 1. To validate the PA-based ablated lesion visualization, sham imaging procedures based on two illumination modes were performed at regions not containing the ablated tissue as the negative control. For cross-validating two illumination modes, both modes were performed at the same ablated tissue plane. US scanning was performed at the same location before the PA imaging to acquire the anatomical information. In the repetitive illumination (3WL-Rep) mode, wavelengths of 740 nm, 760 nm, and 780 nm were used, capturing the local spectrum peak appearing in the non-ablated tissue at 760 nm. In the individual wavelength illumination (16WL-Indiv) mode, the wavelength range of 700 nm to 850 nm was used with a step of 10 nm.

Table 1. Experimental Conditions

	Experiment	Imaging Tissue Region	Ablation	US Scanning	Illumination Mode	Results
#1	**Fast - Sham**	Region 1	No	Yes	3WL-Rep	Figure 5, 6
#2	**Robust - Sham**	Region 2	No	Yes	16WL-Indiv	Figure 7
#3	**Fast - Ablation**	Region 3	Yes	Yes	3WL-Rep	Figure 5, 6
#4	**Robust - Ablation**	Region 3	Yes	Yes	16WL-Indiv	Figure 7

4. Results

4.1. *In Vivo* Visualization of a beating heart

The repetitive illumination of three wavelengths, 740 nm, 760 nm, and 780 nm, was performed as the fast scanning mode to distinguish two tissue types during the presence of the dynamic heartbeat motion. Figure 5 shows the CG-sPA image using the repetitive illumination mode with a particular timing in a cardiac cycle. 90 seconds of sPA images are used for CG algorithm. The image displayed the clear boundary of the cardiac tissue surface, aligning with the US image acquired at the same location and same timing. From the spectral decomposed images, the ablated region was depicted on the expected ablated spot, while most of the PA signals in the other regions were identified as non-ablated tissue. The NE map also showed a strong ablation-induced necrotic extent value in the ablated region. The ablated region containing ablated tissue contrasts can be distinguished from the surrounding non-ablated tissue by the colormap in the NE map (Figure 5).

A sham procedure was performed on a non-ablated region of the swine heart to validate the system specificity confirming that the algorithm can identify the non-ablated tissue as non-ablated contrast. The same parameters used in the ablated tissue imaging session were used to acquire and process data. As the result, no obvious ablated contrast was detected. Most of the sPA signals were identified as the non-ablated tissue contrast. The NE mapping further confirms the non-ablated tissue identification.

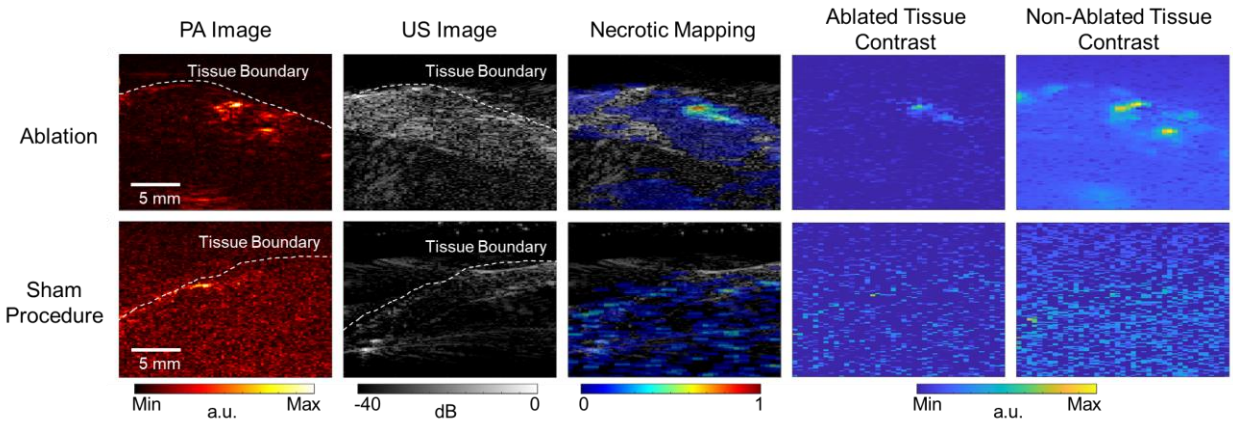

Figure 5. CG-sPA imaging results of the *in vivo* beating heart based on repetitive illumination. The ablated and non-ablated tissue contrast maps show the outcome of the spectroscopic decomposition algorithm. The sham procedure was performed in a slice not containing ablated tissue. The displayed PA images were acquired with 740 nm wavelength.

To demonstrate the temporal variation of sPA based necrotic mapping in the *in vivo* beating heart, Figure 6 displays the CG-sPA images of an entire cardiac cycle, also available as Movie 1. The position of PA contrast from tissue consistently moved along with the cardiac surface imaged by US imaging, while NE mapping from CG-sPA imaging highlights the ablated lesion at the center ablated area. The same tissue motion trends were observed in the sham procedure with only non-ablated tissue spectrum detected in NE mapping. Note that one heart cycle duration of 2.4 seconds presented is slower than the regular cardiac cycle duration of a swine. This is attributed to hyperthermia due to time lapse after the open chest procedure.

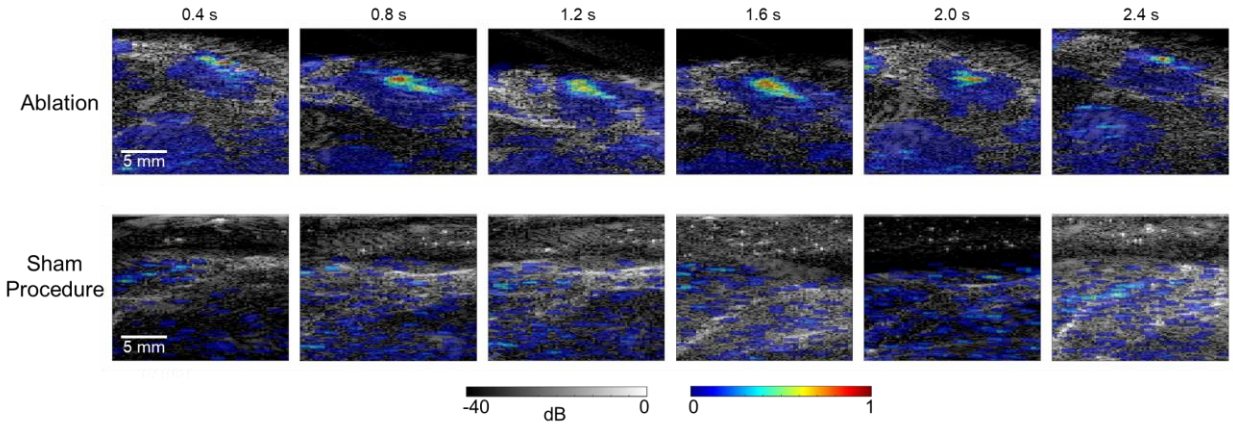

Figure 6. Necrotic extent mapping with repetitive illumination mode in one complete cardiac cycle, also available as Movie 1.

4.2. Cross-Validation with Individual Wavelength Illumination

To evaluate the validity of the fast three-wavelength illumination, we performed individual wavelength illumination scanning using 16 wavelengths capturing the wider spectrum of the cardiac tissue. The wavelength range of 700 nm to 850 nm was used, matching the reported cardiac ablation spectrum range [36]. A wider spectral range is expected to offer a more robust spectroscopic decomposition output by inputting more number of wavelengths. To maximize the PA contrast from the recorded dataset, we calculated the number of frames available for averaging at each CG and selected the CG containing the maximum number of available frames for presenting the NE mapping evaluation. The results from the individual wavelength illumination mode are displayed in Figure 7.

This imaging session was performed right after the repetitive illumination imaging session so that the same location was imaged with equivalent conditions. The NE mapping based on individual wavelength illumination highlighted the same region depicted in the result from repetitive illumination. From the spectroscopic decomposed contrast results, ablated tissue contrast was visible in the ablated tissue area, while non-ablated tissue contrast appeared throughout the tissue. The results from the sham procedure only capture non-ablated tissue contrast. Note that the sham procedures were performed at the different regions between repetitive illumination and individual wavelength illumination sessions.

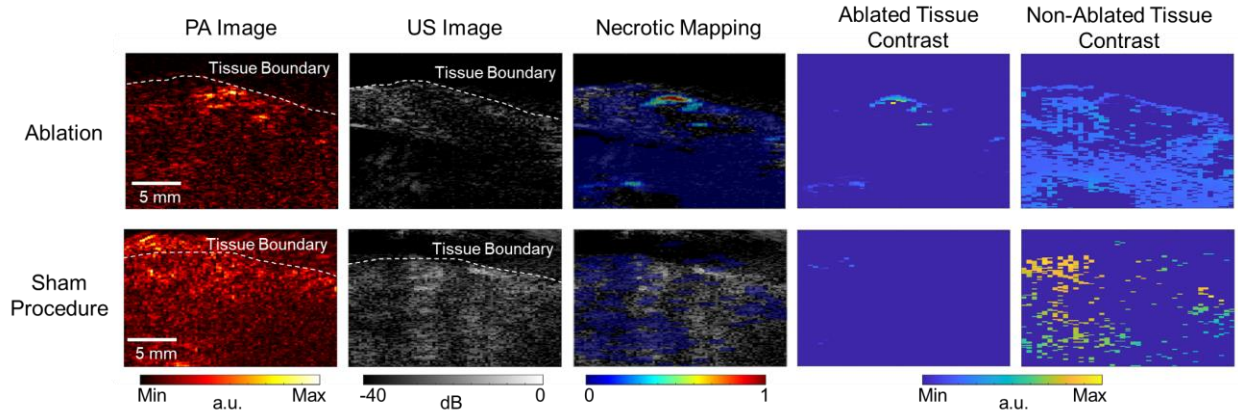

Figure 7. CG-sPA imaging results of the *in vivo* beating heart based on individual wavelength illumination. The ablated and non-ablated tissue contrast maps show the outcome of the spectroscopic decomposition algorithm. The sham procedure was performed in a slice not containing ablated tissue. The displayed PA images were acquired with 740 nm wavelength.

4.3. Histological Validation

A histological comparison was performed between the necrosis region detected in CG-sPA imaging and the actual ablated tissue region of the heart sample to evaluate the accuracy of quantifying the geometry of the ablation-induced tissue necrosis. The cardiac tissue containing the ablated lesion was dissected after the swine was euthanized. The tissue sample was processed by 2,3,5-Triphenyltetrazolium chloride (TTC) to enhance the visibility of the ablated lesion. TTC is a marker of metabolic function and represents a reliable indicator of damaged areas in experimental models. It is a colorless water-soluble dye that is reduced by the mitochondrial enzyme succinate dehydrogenase of living cells into a water-insoluble, light-sensitive compound (formazan) that turns normal (non-ablated) tissue deep red. In contrast, damaged (ablated) tissue

remains white showing the absence of living cells, and thereby indicating the damaged region. As shown in Figure 8, the measured dimension of the ablated region was 6.0 mm in the width and 2.5 mm in the depth. In the NE mapping, the dimension of the ablated lesion (NE > 0.2) scanned in the repetitive illumination scanning mode was 6.01 ± 2.35 mm in width and 1.79 ± 0.75 mm in depth. The dimension in the individual wavelength illumination scanning mode was 5.59 mm in the width and 1.49 mm in the depth.

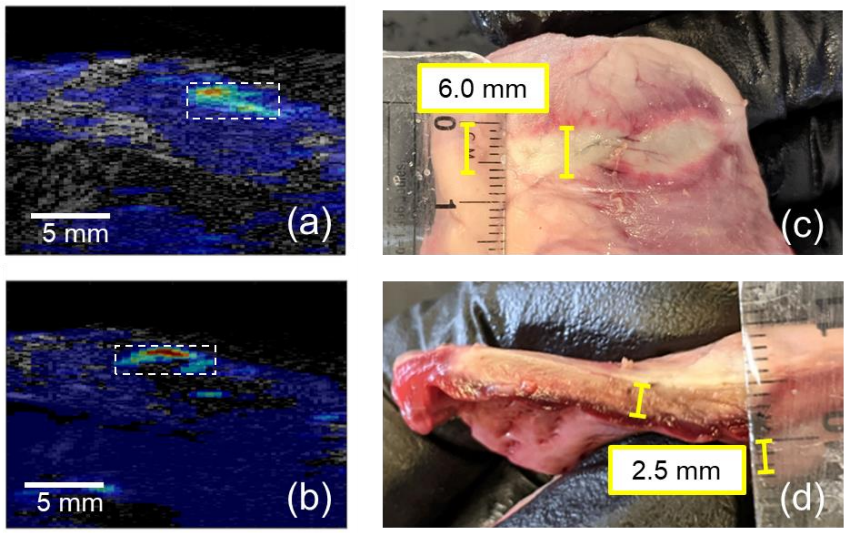

Figure 8. Histology analysis of the ablated tissue region. (a) Ablated region (white dot rectangular) identified by the repetitive illumination scanning mode (b) Ablated region (white dot rectangular) identified by the individual wavelength illumination scanning mode. (c) Top view of the post-procedure processed ablated tissue for width measurement, (d) Side-view of the ablated tissue for depth measurement.

4.4. Evaluation of Imaging Duration

The proposed CG-sPA imaging algorithm uses the averaging filter to enhance the SNR and improve the outcome quality. However, using a long averaging filter compromises the system's real-time imaging potential by requiring a large number of image frames as input. Therefore, we evaluated the impact of the averaging filter sample size on the system accuracy, in terms of sensitivity to ablated tissue identification (false-negative) and its specificity to non-ablated tissue identification (false-positive). This evaluation allows us to understand the required frame duration to grant acceptable performance for future applications. In Figure 9, the NE mappings using data from varied durations of PA recording time are shown. The input data size is displayed in both time duration of the sPA recording, as well as the mean number of frames for averaging after CG across wavelengths. With a greater number of sample frames used for averaging, the ablated lesion in the NE mapping got clearer as the noise reduced. The algorithm sensitivity was high with a smaller sample size where the necrotic region was detected. The small frame size presented the low specificity due to high noise in the non-ablated region. The specificity was enhanced as the input data size increased.

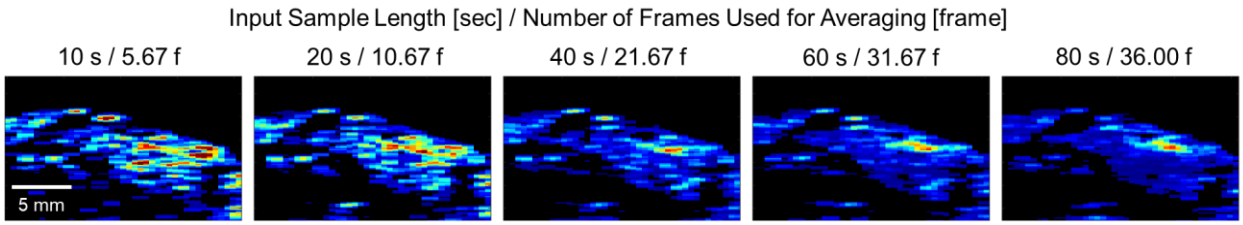

Figure 9. Necrotic extent mapping calculated with a varied input data length in terms of the time duration of the collected data and their mean number of frames used for averaging across wavelengths.

Figure 10 presents the quantification of the NE map accuracy variation under different sample input sizes. The areas selected to quantify the NE value in the ablation region (ABL) and background non-ablated region (NAB) are shown in Figure 10 (a). The averaged NE value within these two marked regions was selected to represent and quantify the sensitivity and specificity of the necrotic lesion identification, respectively (Figure 10 (b)). The ABL region value reaches stable status 30 seconds of input data length. Meanwhile, the NAB region value converges to zero, indicating the state of non-ablated tissue. Further, the ratio of the mean NE values between two regions was calculated to represent the ablated tissue detectability contrast (Figure 10 (c)). The NE ratio continuously increased with the increment of input data.

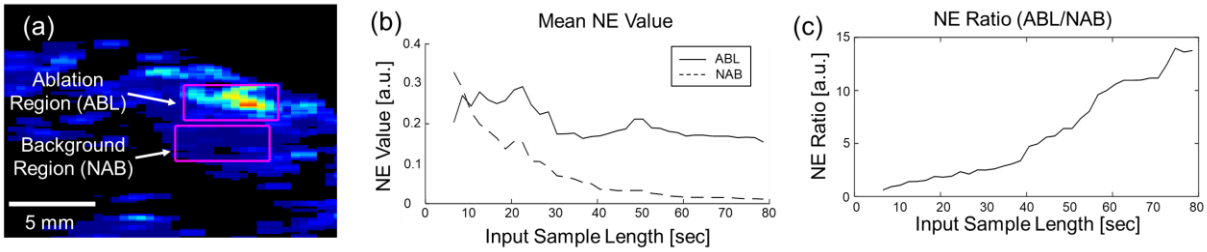

Figure 10. Quantitative evaluation of NE mapping accuracy variation under varied input data duration. (a) A NE map based on 80 seconds of input data under repetitive illumination mode. Ablation (ABL) and background non-ablation (NAB) regions are marked. (b) The mean NE value in the ABL and NAB regions changes over varied input data duration. (c) The ratio of NE values between two regions changes over varied input data duration.

5. Discussion

The proposed CG sPA imaging in the repetitive illumination mode was able to visualize the ablated lesion in a beating heart. A boundary based on the NE value was able to isolate the ablated lesion from the non-ablated counterpart. The PA contrast was generally lower in the sham procedure compared to the condition including the ablated lesion, which led to higher background noise. Despite the noise, the NE mapping was not suffered from the low SNR and presented non-ablated tissue distribution correctly. These observations demonstrate the robustness of the CG sPA imaging and NE mapping. By processing NE mapping in the temporal axis throughout a cardiac cycle, it was observed the ablated lesion moved along the heartbeat corresponding to the shift of the cardiac tissue surface. While the lesion was consistently visible, the dimension of the ablated lesion varied between different timings in a cardiac cycle. This is attributed to two factors. First, the SNR of the ablated lesion may be temporally inhomogeneous because the amount of light illumination dose varies as the position of the cardiac surface changes. Second, due to the nature of the heartbeat, the cardiac tissue stays longer time at the close location in the relaxation phase. Therefore, a higher number of imaging frames for averaging was accessible at such timing. This resulted in the variation

of the used number of frames for averaging in a cardiac cycle and affected the accuracy of the mapped NE value.

The results from the individual wavelength illumination scanning confirmed the ablation-induced necrotic lesion, aligning with the observation from the repetitive illumination scanning. The consistent visualization of the lesion supports the use of less number of wavelengths in repetitive illumination compared to the thorough spectral illumination of 16 wavelengths in individual wavelength illumination. Regardless of the significantly higher number of wavelengths used, the decomposed contrasts between the two illumination modes were not considerably different because each wavelength only covers PA images less than two cardiac cycles in the individual illumination mode, resulting in less frame averaging in the CG sPA processing. In fact, the tissue boundary was less clear in the sPA image in the sham dataset (Figure 7). Still, it did not affect the non-ablated tissue identification in the NE mapping.

The histology analysis presented the necrotic lesion boundary identification capability with the CG-sPA imaging method. Both illumination modes showed a high agreement, especially in the lesion width measurement. The repetitive illumination scanning mode showed a better performance in depth-dimensional measurement, in that a smaller number of frames was used in frame averaging in the individual wavelength illumination scanning mode, as discussed earlier. The degradation in contrast was more eminent in the depth axis due to the light scattering in tissue. This resulted in a higher residual error at a deeper region during spectroscopic decomposition.

The evaluation of the effect of frame duration used in the CG-sPA imaging process on the resulted necrotic mapping offers guidance for future real-time implementation. We quantified the accuracy of identifying ablated and non-ablated regions as the data length changes, indicating the system tolerance to the short-duration data. The detection of the ablated tissue was achieved with less than 10 seconds of input data, supporting the high sensitivity of the algorithm. On the contrary, the non-ablated region identification was less straightforward due to the noise when a short duration of data (e.g. 10 seconds) was used. The false-positive detection was observed on both ablated and non-ablated regions with short duration of data input. Overestimation of the NE value could lead to guide incomplete ablation during the procedure. The trend of suppression of false-positive when the input size increased matches the observation in Figure 9.

Despite the successful demonstration of the necrotic lesion visualization in the *in vivo* beating heart, we recognize several limitations in the current results and the method. First, the ablation and its imaging were performed at the external surface of the heart instead of in an intracardiac environment. Our simplified experimental setup allows us to focus on evaluating *in vivo* imaging capabilities by eliminating the factors such as the difficulty of aligning the imaging setup with the ablated lesion, the inhomogeneous light illumination in the intracardiac space, and the light attenuation in a blood-filled condition. Based on the outcome reported in the paper, we will focus on miniaturizing the imaging setup to validate the proposed imaging method in an intracardiac environment. Second, the current CG sPA imaging pipeline does not grant a real-time visualization capability. Considering that a typical ablation process takes less than 1 minute [38–40], the current pipeline does not allow capturing the tissue type transition in real-time. While the current in vivo CG-sPA system allows the intraoperative evaluation of the ablated tissue, the real-time intra-ablation monitoring has not been realized. Increasing the imaging speed requires improving the SNR with less data duration. A high-speed laser with 100 Hz [41] or higher pulse repetition frequency increases the data points and can shorten the data recording time. Improving beamforming and spectroscopic decomposition algorithm will also contribute to achieving real-time monitoring.

6. Conclusions

In this work, *in vivo* visualization of the cardiac ablation region at a beating heart was realized through CG-sPA imaging. Two light illumination modes were implemented to cross-validate the ablation lesion identification capability by using either three or 16 wavelengths. The results from both modes successfully were able to distinguish the ablation-induced necrotic tissue from the surrounding non-ablated tissues with boundaries. The quantified ablated lesion dimension showed an agreement with the gross histological evaluation. Hence, this *in vivo* demonstration strongly supports the potential of PA imaging being used for intraoperative cardiac ablation guidance.

Acknowledgments

This work was supported by the Worcester Polytechnic Institute internal fund, the Transformative Research and Innovation, Accelerating Discovery (TRIAD) grant, and the National Institutes of Health funding [grant numbers CA134675, OD028162, R01EB022011]. We thank the Johns Hopkins University Animal Care and Use Committee for their assistance with this study.

Disclaimer of Competing Interest

Tommaso Mansi is scientist and employee of Janssen: Pharmaceutical Companies of Johnson & Johnson. Young-Ho Kim and Florin-Cristian Ghesu are scientists and employees of Siemens Healthineers USA. The other authors have no known competing financial interests or personal relationships that could have appeared to influence the work reported in this paper.

Disclaimer

The concepts and information presented in this paper are based on research results that are not commercially available. Future availability cannot be guaranteed.

Reference

[1] Atrial Fibrillation | cdc.gov, (n.d.). https://www.cdc.gov/heartdisease/atrial_fibrillation.htm (accessed January 19, 2022).

[2] C.A. Morillo, A. Banerjee, P. Perel, D. Wood, X. Jouven, Atrial fibrillation: The current epidemic, J. Geriatr. Cardiol. 14 (2017) 195–203. https://doi.org/10.11909/j.issn.1671-5411.2017.03.011.

[3] D.C. Peters, J. V. Wylie, T.H. Hauser, R. Nezafat, Y. Han, J.J. Woo, J. Taclas, K. V. Kissinger, B. Goddu, M.E. Josephson, W.J. Manning, Recurrence of Atrial Fibrillation Correlates With the Extent of Post-Procedural Late Gadolinium Enhancement. A Pilot Study, JACC Cardiovasc. Imaging. 2 (2009) 308–316. https://doi.org/10.1016/j.jcmg.2008.10.016.

[4] H. Nakagawa, W.M. Jackman, The role of contact force in atrial fibrillation ablation, J. Atr. Fibrillation. 7 (2014) 78–84. https://doi.org/10.4022/jafib.1027.

[5] A. Santoro, A. Romano, F. Lamberti, Steam pop during cavo-tricuspid isthmus ablation shown by

intracardiac echocardiography, J. Cardiol. Cases. 23 (2021) 13–15. https://doi.org/10.1016/j.jccase.2020.08.002.

[6] R.A. Kruger, P. Liu, Y. “Richard” Fang, C.R. Appledorn, Photoacoustic ultrasound (PAUS)—Reconstruction tomography, Med. Phys. 22 (1995) 1605–1609. https://doi.org/10.1118/1.597429.

[7] R.O. Esenaliev, A.A. Karabutov, F.K. Tittel, B.D. Fornage, S.L. Thomsen, C. Stelling, A.A. Oraevsky, Laser optoacoustic imaging for breast cancer diagnostics: limit of detection and comparison with x-ray and ultrasound imaging</title>, in: B. Chance, R.R. Alfano (Eds.), Opt. Tomogr. Spectrosc. Tissue Theory, Instrumentation, Model. Hum. Stud. II, SPIE, 1997: pp. 71–82. https://doi.org/10.1117/12.280213.

[8] C.G.A. Hoelen, F.F.M. de Mul, R. Pongers, A. Dekker, Three-dimensional photoacoustic imaging of blood vessels in tissue, Opt. Lett. 23 (1998) 648. https://doi.org/10.1364/ol.23.000648.

[9] J. Yao, L. V. Wang, Photoacoustic microscopy, Laser Photonics Rev. 7 (2013) 758–778. https://doi.org/10.1002/lpor.201200060.

[10] P. Beard, Biomedical photoacoustic imaging Review, Interface Focus. 1 (2011) 602–631. https://doi.org/10.1098/rsfs.2011.0028.

[11] Y. Matsumoto, Y. Asao, A. Yoshikawa, H. Sekiguchi, M. Takada, M. Furu, S. Saito, M. Kataoka, H. Abe, T. Yagi, K. Togashi, M. Toi, Label-free photoacoustic imaging of human palmar vessels: a structural morphological analysis, Sci. Reports 2018 81. 8 (2018) 1–8. https://doi.org/10.1038/s41598-018-19161-z.

[12] S. Hu, Neurovascular photoacoustic tomography, Front. Neuroenergetics. (2010). https://doi.org/10.3389/fnene.2010.00010.

[13] C. Kim, C. Favazza, L. V. Wang, In vivo photoacoustic tomography of chemicals: High-resolution functional and molecular optical imaging at new depths, Chem. Rev. 110 (2010) 2756–2782. https://doi.org/10.1021/cr900266s.

[14] S. Hu, L. V. Wang, Photoacoustic imaging and characterization of the microvasculature, J. Biomed. Opt. 15 (2010) 011101. https://doi.org/10.1117/1.3281673.

[15] S. Gao, M.C. Flegal, H.K. Zhang, Feasibility of laparoscopic photoacoustic imaging system based on diffusing side-illumination fibers, in: A.A. Oraevsky, L. V. Wang (Eds.), Photons Plus Ultrasound Imaging Sens. 2022, SPIE, 2022: p. 94. https://doi.org/10.1117/12.2613895.

[16] J. Zhang, F. Duan, Y. Liu, L. Nie, High-resolution photoacoustic tomography for early-stage cancer detection and its clinical translation, Radiol. Imaging Cancer. 2 (2020). https://doi.org/10.1148/RYCAN.2020190030/ASSET/IMAGES/LARGE/RYCAN.2020190030.FIG6.JPEG.

[17] M. Mehrmohammadi, S.J. Yoon, D. Yeager, S.Y. Emelianov, Photoacoustic Imaging for Cancer Detection and Staging, Curr Mol Imaging. 27 (2013) 1–19. https://doi.org/10.1037/a0032811.Child.

[18] H.K. Zhang, Y. Chen, J. Kang, A. Lisok, I. Minn, M.G. Pomper, E.M. Boctor, Prostate-specific membrane antigen-targeted photoacoustic imaging of prostate cancer in vivo, J. Biophotonics. 11 (2018) 1–6. https://doi.org/10.1002/jbio.201800021.

[19] E. Merčep, X.L. Deán-Ben, D. Razansky, Imaging of blood flow and oxygen state with a multi-segment optoacoustic ultrasound array, Photoacoustics. 10 (2018) 48–53. https://doi.org/10.1016/J.PACS.2018.04.002.

[20] M.L. Li, J.T. Oh, X. Xie, G. Ku, W. Wang, C. Li, G. Lungu, G. Stoica, L. V. Wang, Simultaneous molecular and hypoxia imaging of brain tumors in vivo using spectroscopic photoacoustic tomography, Proc. IEEE. 96 (2008) 481–489. https://doi.org/10.1109/JPROC.2007.913515.

[21] M. Wu, G. Springeling, M. Lovrak, F. Mastik, S. Iskander-Rizk, T. Wang, H.M.M. van Beusekom, A.F.W. van der Steen, G. Van Soest, Real-time volumetric lipid imaging in vivo by intravascular photoacoustics at 20 frames per second, Biomed. Opt. Express. 8 (2017) 943. https://doi.org/10.1364/boe.8.000943.

[22] Y. Cao, J. Hui, A. Kole, P. Wang, Q. Yu, W. Chen, M. Sturek, J.X. Cheng, High-sensitivity intravascular photoacoustic imaging of lipid-laden plaque with a collinear catheter design, Sci. Rep. 6 (2016) 1–8. https://doi.org/10.1038/srep25236.

[23] B. Wang, A. Karpiouk, D. Yeager, J. Amirian, S. Litovsky, R. Smalling, S. Emelianov, Intravascular photoacoustic imaging of lipid in atherosclerotic plaques in the presence of luminal blood, Opt. Lett. 37 (2012) 1244. https://doi.org/10.1364/ol.37.001244.

[24] K. Jansen, M. Wu, A.F.W. van der Steen, G. van Soest, Lipid detection in atherosclerotic human coronaries by spectroscopic intravascular photoacoustic imaging, Opt. Express. 21 (2013) 21472. https://doi.org/10.1364/oe.21.021472.

[25] J. Zhang, S. Yang, X. Ji, Q. Zhou, D. Xing, Characterization of lipid-rich aortic plaques by intravascular photoacoustic tomography: Ex vivo and in vivo validation in a rabbit atherosclerosis model with histologic correlation, J. Am. Coll. Cardiol. 64 (2014) 385–390. https://doi.org/10.1016/j.jacc.2014.04.053.

[26] M.U. Arabul, M. Heres, M.C.M. Rutten, M.R. van Sambeek, F.N. van de Vosse, R.G.P. Lopata, Toward the detection of intraplaque hemorrhage in carotid artery lesions using photoacoustic imaging, J. Biomed. Opt. 22 (2016) 041010. https://doi.org/10.1117/1.jbo.22.4.041010.

[27] J.-W. Muller, R. van Hees, M. van Sambeek, P. Boutouyrie, M. Rutten, P. Brands, M. Wu, R. Lopata, Towards in vivo photoacoustic imaging of vulnerable plaques in the carotid artery, Biomed. Opt. Express. 12 (2021) 4207. https://doi.org/10.1364/boe.430064.

[28] M. Graham, F. Assis, D. Allman, A. Wiacek, E. Gonzalez, M. Gubbi, J. Dong, H. Hou, S. Beck, J. Chrispin, M.A.L. Bell, In vivo demonstration of photoacoustic image guidance and robotic visual servoing for cardiac catheter-based interventions, IEEE Trans. Med. Imaging. 39 (2020) 1015–1029. https://doi.org/10.1109/TMI.2019.2939568.

[29] R. Bouchard, N. Dana, L. Di Biase, A. Natale, S. Emelianov, Photoacoustic characterization of radiofrequency ablation lesions, in: Photons Plus Ultrasound Imaging Sens. 2012, SPIE, 2012: p. 82233K. https://doi.org/10.1117/12.909161.

[30] N. Dana, L. Di Biase, A. Natale, S. Emelianov, R. Bouchard, In vitro photoacoustic visualization of myocardial ablation lesions, Hear. Rhythm. 11 (2014) 150–157. https://doi.org/10.1016/j.hrthm.2013.09.071.

[31] S. Iskander-Rizk, P. Kruizinga, A.F.W. van der Steen, G. van Soest, Spectroscopic photoacoustic imaging of radiofrequency ablation in the left atrium, Biomed. Opt. Express. 9 (2018) 1309. https://doi.org/10.1364/boe.9.001309.

[32] S. Iskander-Rizk, G. Springeling, P. Kruizinga, R.H.S.H. Beurskens, A.F.W. Van Der Steen, G. Van Soest, Photoacoustic-Enabled RF Ablation Catheters for Lesion Monitoring, in: IEEE Int. Ultrason. Symp. IUS, IEEE Computer Society, 2018. https://doi.org/10.1109/ULTSYM.2018.8579858.

[33] S. Iskander-Rizk, P. Kruizinga, R. Beurskens, G. Springeling, F. Mastik, N.M.S. de Groot, P. Knops, A.F.W. van der Steen, G. van Soest, Real-time photoacoustic assessment of radiofrequency ablation lesion formation in the left atrium, Photoacoustics. 16 (2019) 100150. https://doi.org/10.1016/j.pacs.2019.100150.

[34] H.K. Zhang, Y. Chen, J. Kang, A. Lisok, I. Minn, M.G. Pomper, E.M. Boctor, Prostate-specific membrane antigen-targeted photoacoustic imaging of prostate cancer in vivo, J. Biophotonics. 11 (2018) e201800021. https://doi.org/10.1002/jbio.201800021.

[35] M. Li, Y. Tang, J. Yao, Photoacoustic tomography of blood oxygenation: A mini review, Photoacoustics. 10 (2018) 65–73. https://doi.org/10.1016/j.pacs.2018.05.001.

[36] S. Gao, H. Ashikaga, T. Mansi, H.R. Halperin, H.K. Zhang, Photoacoustic Necrotic Region Mapping for Radiofrequency Ablation Guidance, in: IEEE Int. Ultrason. Symp. IUS, IEEE, 2021: pp. 1–4. https://doi.org/10.1109/IUS52206.2021.9593388.

[37] S. Gao, R. Tsumura, D.P. Vang, K. Bisland, K. Xu, Y. Tsunoi, H.K. Zhang, Acoustic-resolution photoacoustic microscope based on compact and low-cost delta configuration actuator, Ultrasonics. 118 (2021) 106549. https://doi.org/10.1016/j.ultras.2021.106549.

[38] R.A. Winkle, S. Mohanty, R.A. Patrawala, R.H. Mead, M.H. Kong, G. Engel, J. Salcedo, C.G. Trivedi, C. Gianni, P. Jais, A. Natale, J.D. Day, Low complication rates using high power (45–50 W) for short duration for atrial fibrillation ablations, Hear. Rhythm. 16 (2019) 165–169. https://doi.org/10.1016/j.hrthm.2018.11.031.

[39] V.Y. Reddy, D. Shah, J. Kautzner, B. Schmidt, N. Saoudi, C. Herrera, P. Jaïs, G. Hindricks, P. Peichl, A. Yulzari, H. Lambert, P. Neuzil, A. Natale, K.H. Kuck, The relationship between contact force and clinical outcome during radiofrequency catheter ablation of atrial fibrillation in the TOCCATA study, Hear. Rhythm. 9 (2012) 1789–1795. https://doi.org/10.1016/j.hrthm.2012.07.016.

[40] V.Y. Reddy, S.R. Dukkipati, P. Neuzil, A. Natale, J.P. Albenque, J. Kautzner, D. Shah, G. Michaud, M. Wharton, D. Harari, S. Mahapatra, H. Lambert, M. Mansour, Randomized, Controlled Trial of the Safety and Effectiveness of a Contact Force-Sensing Irrigated Catheter for Ablation of Paroxysmal Atrial Fibrillation: Results of the TactiCath Contact Force Ablation Catheter Study for Atrial Fibrillation (TOCCASTAR) S, Circulation. 132 (2015) 907–915. https://doi.org/10.1161/CIRCULATIONAHA.114.014092.

[41] H. Gyun Lim, U. Jung, J. Hyuck Choi, H. Tae Choo, G. Ug Kim, J. Ryu, H. Choi, Fully Customized Photoacoustic System Using Doubly Q-Switched Nd:YAG Laser and Multiple Axes Stages for Laboratory Applications, Sensors 2022, Vol. 22, Page 2621. 22 (2022) 2621. https://doi.org/10.3390/S22072621.